

Non-Hermitian Skin Effect in Periodically-Driven Dissipative Ultracold Atoms

Zhao-Fan Cai,¹ Tao Liu,^{1,*} and Zhongmin Yang^{1,2,3,†}

¹*School of Physics and Optoelectronics, South China University of Technology, Guangzhou 510640, China*

²*Research Institute of Future Technology, South China Normal University, Guangzhou 510006, China*

³*State Key Laboratory of Luminescent Materials and Devices and Institute of Optical Communication Materials, South China University of Technology, Guangzhou 510640, China*

(Dated: January 16, 2025)

The non-Hermitian skin effect (NHSE), featured by the collapse of bulk-band eigenstates into the localized boundary modes of the systems, is one of most striking properties in the fields of non-Hermitian physics. Unique physical phenomena related to the NHSE have attracted a lot of interest, however, their experimental realizations usually require nonreciprocal hopping, which faces a great challenge in ultracold-atom systems. In this work, we propose to realize the NHSE in a 1D optical lattice by periodically-driven ultracold atoms in the presence of staggered atomic loss. By studying the effective Floquet Hamiltonian in the high-frequency approximation, we reveal the underlying mechanism for the periodic-driving-induced the NHSE. We found that the robust NHSE can be tuned by driving phase, which is manifested by the dynamical localization. Most remarkably, we uncover the periodic-driving-induced critical skin effect for two coupled chains with different driving phases, accompanied by the appearance of size-dependent topological in-gap modes. Our studies provide a feasible way for observing the NHSE and exploring corresponding unique physical phenomena due to the interplay of non-Hermiticity and many-body statistics in ultracold-atom systems.

I. INTRODUCTION

Non-Hermitian systems exhibit many unique physical phenomenon without Hermitian counterparts, which have drawn extensive research interest in recent years^{1–43}. In particular, one of their striking physical properties is the emergence of the non-Hermitian skin effect (NHSE)^{7–12,26–31}. By the NHSE, an extensive number of bulk modes collapse into localized boundary modes in the open boundaries. The NHSE has its intrinsic topological origin associated to the point gap^{23,30}, and it can lead to many exotic physical phenomena, e.g., breakdown of conventional Bloch band theory^{7–9}, nonunitary scaling of non-Hermitian localization⁴⁴, and entanglement phase transitions³⁹.

Although several theoretical proposals have devoted to exploring the NHSEs and several related novel physical phenomena^{34,43,45}, experimental studies remained largely fall behind. The main obstacle, in most cases, is the challenging requirement of the nonreciprocal hopping in achieving the NHSE for many experimental platforms. At present, most experiments are limited to classical phononic and optical structures^{46–48}, and electrical circuits^{49,50}. A more operational approach is to utilize onsite gain and loss or equivalently imbalanced onsite dissipation^{31,35,38,51,52}.

Ultracold quantum gases in optical lattices provide a promising platform for studying intriguing quantum physics due to their high controllability, rich lattice structures and many-body nature^{53–56}, which have been widely utilized to explore topological phases^{54,55} and many-body physics⁵⁶. Furthermore, NHSEs have been theoretically proposed^{51,57,58} and also experimentally observed^{38,52} in optical lattices of ultracold atoms. These studies usually rely on complicated lattice structures to achieve the NHSE assisted by atomic loss.

Alternatively, we may realize the NHSE and study the associated physical phenomena in an experimentally accessible optical lattice of ultracold atoms based on Floquet engineering. Floquet engineering is a versatile tool by tailoring a system using the periodic driving, and has produced a wide variety of fascinating physics in the field of ultracold atoms due to their excellent dynamic control^{59–63}. Most recently, loss induced NHSEs have been reported in periodically-driven photonic structure⁶⁴ and acoustic metamaterial⁶⁵. Both proposals are classical settings, and it is natural to achieve the NHSE in periodically driven ultracold-atom systems, which would offer an exciting opportunity for studying the NHSE and its interplay with many-body interaction.

In this paper, we theoretically propose to realize the NHSE in periodically-driven dissipative ultracold atoms. By periodically driving the 1D optical lattice of ultracold atoms in the presence of the staggered atomic loss, we observe the NHSE with all the modes localized at boundaries, which can be manifested by dynamical localization. The direction of the skin-mode localization can be controlled by the driving phase, and characterized by the winding number. Moreover, by coupling two periodically-driven chains with different driving phases, we study the critical skin effect, with the appearance of size-dependent topological in-gap modes.

The rest of this paper is organized as follows. In Sec. II(A,B), we present a 1D optical lattice constructed by dissipative ultracold atoms under the periodic modulation of onsite potential. When the staggered atomic loss is introduced along the chain, we observe the NHSE. We discuss the effect of disorder and dynamical localization in Sec. II(C) and Sec. II(D). To go further for demonstrating the novel non-Hermitian physics in periodically driven system, we study the critical skin effect in Sec. III. Finally, we summarize the key findings

in Sec. IV.

II. PERIODICALLY-DRIVEN DISSIPATIVE ULTRACOLD ATOMS

A. Model and Floquet Hamiltonian

To induce NHSE, we consider periodically-driven dissipative quantum systems, which can be experimentally realized by using well-developed techniques of Floquet engineering in ultracold atoms, including the approaches of lattice shaking, laser-assisted tunneling, modulation of external field gradients and a combination of these methods^{59–63}. In 1D dissipative ultracold atoms, by periodic modulation of onsite potential in 1D optical lattices in a tilted optical lattice (see Fig. 1), we construct the periodically-driven Hamiltonian $\mathcal{H}_p(t) = \mathcal{H}_0 + \mathcal{H}_d(t)$, with

$$\mathcal{H}_0 = -J \sum_{j=1}^{L-1} (c_{j+1}^\dagger c_j + \text{H.c.}) - i\lambda \sum_{j=1}^{L/2} n_{2j} - i\lambda_1 \sum_{j=1}^L n_j, \quad (1)$$

$$\mathcal{H}_d(t) = \sum_{j=1}^L F \left[\cos(\omega t + \phi) j + \sin(\omega t) \frac{3 + (-1)^j}{2} \right] n_j. \quad (2)$$

Here, \mathcal{H}_0 is the undriven Hamiltonian in presence of staggered dissipation with λ_1 and $\lambda_2 = \lambda_1 + \lambda$ being atomic loss rate at odd and even sites (see Fig. 1), and \mathcal{H}_d represents periodically-modulated onsite potential in a tilted optical lattice, with its first term being onsite energy offset along the lattice, and its second term being staggered onsite potential. c_j^\dagger is the creation operator at the j th lattice site, $n_j = c_j^\dagger c_j$ is corresponding density operator, F , ω , and ϕ are driving strength, frequency and phase, and J is atomic hopping rate. The details of experimental proposals are shown in Appendix A. Without loss of generality, we set $\lambda_1 = 0$ below.

By performing an unitary transformation $\mathcal{U}(t) = \exp\left(i \int^t \mathcal{H}_d(t') dt'\right)$ to a rotating frame of reference (see Appendix B), \mathcal{H}_p is rewritten as

$$\mathcal{H}(t) = \sum_j \left[(uc_{2j}^\dagger c_{2j-1} + vc_{2j+1}^\dagger c_{2j} + \text{H.c.}) - i\lambda n_{2j} \right], \quad (3)$$

where

$$u = -J e^{i\sqrt{2}\alpha \cos(\frac{\phi}{2} + \frac{\pi}{4}) \sin(\omega t + \frac{\phi}{2} - \frac{\pi}{4})}, \quad (4)$$

$$v = -J e^{i\sqrt{2}\alpha \sin(\frac{\phi}{2} + \frac{\pi}{4}) \cos(\omega t + \frac{\phi}{2} - \frac{\pi}{4})}, \quad (5)$$

with $\alpha = \sqrt{2}F/\omega$.

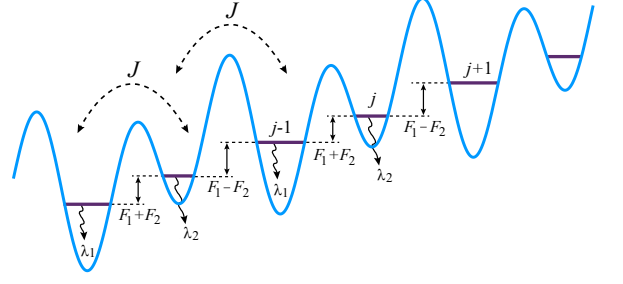


FIG. 1. Schematic showing the tilted optical lattice of ultracold atoms with periodic modulation of onsite potential. The bare atomic tunnel coupling is represented by J , λ_1 and λ_2 with $\lambda_2 = \lambda_1 + \lambda$ denote the staggered atomic loss at odd and even sites, and onsite potential modulations are expressed as $F_1 = F \cos(\omega t + \phi)$, and $F_2 = F \sin(\omega t)$.

According to Floquet theorem⁶⁶, a time-periodic Hamiltonian $\mathcal{H}(t) = \mathcal{H}(t + T)$, with the driving period $T = 2\pi/\omega$, is governed by Schrödinger equation $i\partial_t |\psi_n(t)\rangle = \mathcal{H}(t) |\psi_n(t)\rangle$. There exists a complete set of orthogonal solutions $|\psi_n(t)\rangle = e^{-iE_n t} |u_n(t)\rangle$, with $|u_n(t)\rangle = |u_n(t + T)\rangle$ and quasienergy E_n . In this work, we are interested in the stroboscopic dynamics governed by the time-independent effective Floquet Hamiltonian \mathcal{H}_F , defined as

$$U(T) = \mathcal{T} e^{-i \int_0^T \mathcal{H}(t') dt'} = e^{-i\mathcal{H}_F T}, \quad (6)$$

where \mathcal{T} is the time-ordering operator, and $U(T) |\psi_n(0)\rangle = e^{-iE_n T} |\psi_n(0)\rangle$. Due to the non-Hermiticity of $\mathcal{H}(t)$, the Floquet operator $U(T)$ is not unitary, and the quasienergy E_n can be complex.

B. Non-Hermitian Skin Effect

To reveal the periodically-driven skin effect for the dissipative ultracold-atom system proposed above, we plot the complex quasienergy spectrum E_n and corresponding density distributions $|\psi_n|^2$ of the Floquet Hamiltonian \mathcal{H}_F , as shown in Fig. 2. The quasienergies are calculated under both periodic (PBC) and open (OBC) boundary conditions, while density distributions are under the OBC. The complex quasienergy spectrum of the pure dissipative system with $\alpha = 0$ is insensitive to the boundary conditions, and there exists no NHSE [see Figs. 2(a1,a2)]. In addition, the only periodically-driven ultracold atoms with $\lambda = 0$ cannot induce the NHSE [see Figs. 2(b1,b2)].

For the periodically-driven and dissipative ultracold-atom chain in the presence of the staggered loss (i.e., $\alpha \neq 0$ and $\lambda \neq 0$), the complex quasienergy spectrum is sensitive to boundary conditions [see Figs. 2(c1,d1,e1)]. The periodic drive induces the formation of point gaps, a loop in the complex plane [see red dots in Figs. 2(c1,d1,e1)], encircling the open-arc spectrum

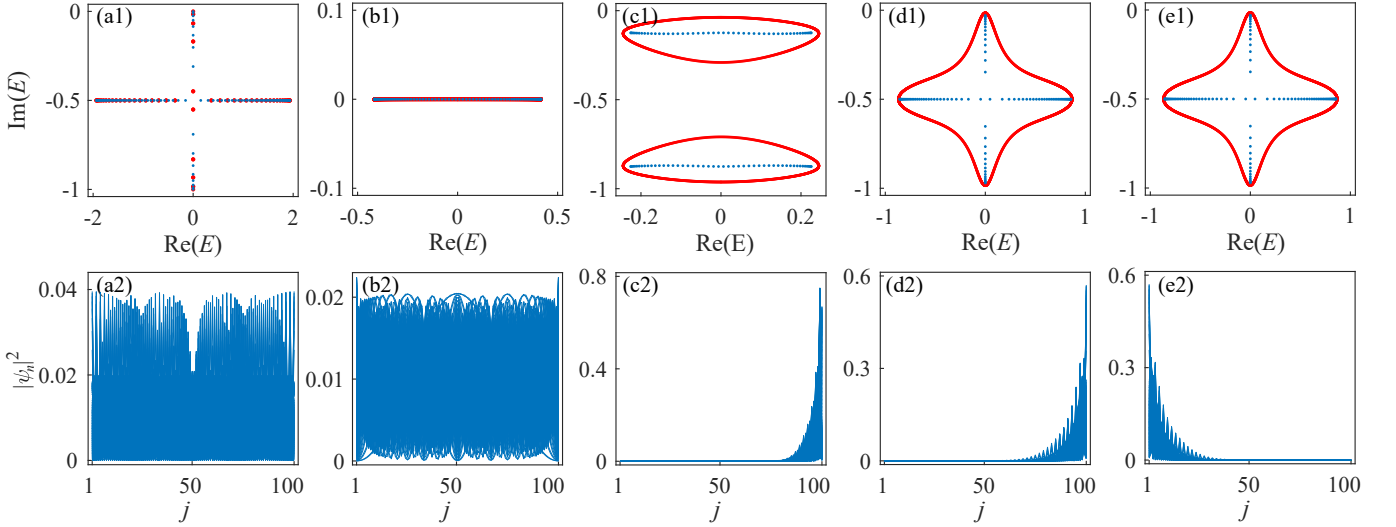


FIG. 2. Complex quasienergy spectrum E_n and corresponding density distributions $|\psi_n|^2$ of the Floquet Hamiltonian \mathcal{H}_F . The red and blue dots indicate the quasienergies under PBC and OBC, respectively. (a1, a2) Pure dissipative ultracold atoms with $\alpha = 0$, and (b1, b2) the only periodic drive with $\alpha = 2$, $\omega = 2\pi$ and $\lambda = 0$. Periodically-driven dissipative ultracold atoms with (c1, c2) $\alpha = 2$, $\omega = 2\pi$ and $\phi = 0$, (d1, d2) $\alpha = 1.5$, $\omega = 3\pi$ and $\phi = 0$, and (e1, e2) $\alpha = 1.5$, $\omega = 3\pi$ and $\phi = \pi$. The other parameters used are $\lambda/J = 1.0$, and $L = 100$.

of OBC (blue dots). Figure 2(c2, d2, e2) plots the density distributions $|\psi_n|^2$ of all the Floquet eigenmodes, where all the modes are localized at the boundaries. Moreover, these non-Hermitian skin modes can be localized at either right [see Figs. 2(c2, d2)] or left [see Figs. 2(e2)] boundaries, determined by the driving phase ϕ . Therefore, our periodic-modulation approach realizes a tunable 1D NHSE in the dissipative ultracold-atom system.

The NHSE has its topological origin, which is characterized by the point-gap topology with the topological invariant of winding number³⁰

$$\mathcal{W}(E_r) = \int_{-\pi}^{\pi} \frac{dk}{2\pi i} \partial_k \ln \det [\mathcal{H}_F(k) - E_r], \quad (7)$$

where $\mathcal{H}_F(k)$ is the Floquet Hamiltonian in momentum space, and E_r is a reference energy point inside the loop of the point gap. $\mathcal{W}(E_r)$ counts the number of times that the complex spectrum of $\mathcal{H}_F(k)$ encircles E_r .

We analytically calculate $\mathcal{W}(E_r)$ by approximating $\mathcal{H}_F(k)$ using the time-independent effective Hamiltonian $\mathcal{H}_{\text{eff}}(k)$, obtained by the Floquet-Magnus expansion in the high-frequency approximation^{67–69}. For $\omega \gg J, F$, the effective Hamiltonian $\mathcal{H}_{\text{eff}}(k)$ (see details in Appendix C) is derived as

$$\begin{aligned} \mathcal{H}_{\text{eff}}(k) = & - \sum_k \left[J J_0(\alpha) (1 + e^{-ik}) c_{k,A}^\dagger c_{k,B} + \text{H.c.} \right] \\ & - s \frac{2J^2 J_{-1}^2(\alpha)}{\omega} \sum_k \sin(k) \left(c_{k,A}^\dagger c_{k,A} - c_{k,B}^\dagger c_{k,B} \right) \\ & - i\lambda \sum_k c_{k,B}^\dagger c_{k,B}, \end{aligned} \quad (8)$$

where A and B denote two sublattice sites in the unit cell due to the staggered loss, $J_m(\alpha)$ is the Bessel function of the first kind, and $s = 1$ (-1) corresponding to $\phi = 0$ (π), corresponding to the rightward (leftward) localization. The winding number is calculated as $\mathcal{W} = -1$ ($\mathcal{W} = 1$) for $\phi = 0$ (π).

To further elucidate the mechanism of Floquet induced NHSE considered here, we write down the real-space effective Hamiltonian in the high-frequency expansion

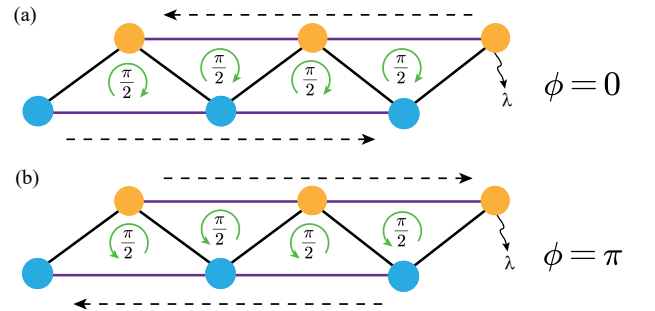


FIG. 3. Schematic showing the 1D zigzag lattice described by Eq. (9). The even sites (yellow filled circles) are dissipated by $\lambda = \lambda_2 - \lambda_1$. A $\pi/2$ magnetic flux threads through each triangular plaquette in clockwise and counter-clockwise directions for (a) $\phi = 0$ and (b) $\phi = \pi$ due to the complex next-nearest-neighbor hopping in Eq. (9). Such a nonzero flux leads to opposite particle transports along the odd and even lattice sites, indicated by the dashed arrows.

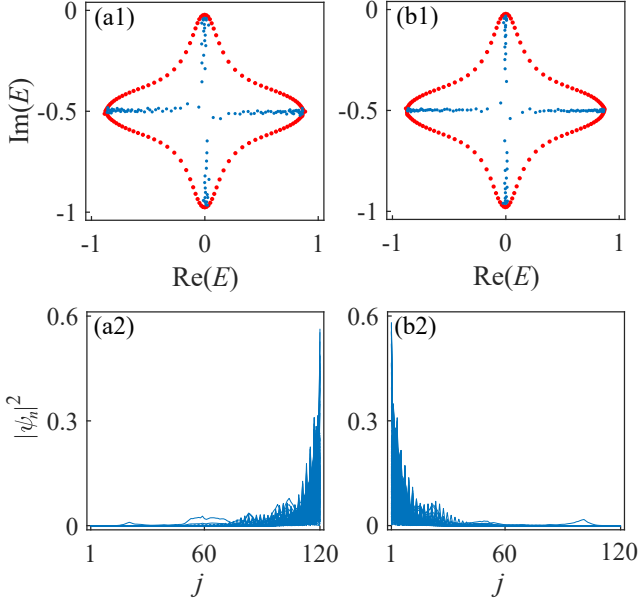


FIG. 4. Complex quasienergy spectrum E_n and corresponding density distributions $|\psi_n|^2$ of the Floquet Hamiltonian \mathcal{H}_F in the presence of onsite disordered potential \mathcal{H}_{dis} for (a1, a2) $\phi = 0$, and (b1, b2) $\phi = \pi$. The red and blue dots indicate the quasienergies under PBC and OBC, respectively. The other parameters used are $\alpha = 1.5$, $\omega = 3\pi$, $\lambda/J = 1$, $W/J = 5$, and $L = 120$.

(see details in Appendix C) as

$$\begin{aligned} \mathcal{H}_{\text{eff}} = & - \sum_j \left[J J_0(\alpha) c_{2j}^\dagger c_{2j-1} + J J_0(\alpha) c_{2j+1}^\dagger c_{2j} + \text{H.c.} \right] \\ & - \sum_j \left[i s \frac{2J^2 J_{-1}^2(\alpha)}{\omega} c_{2j+1}^\dagger c_{2j-1} + \text{H.c.} \right] \\ & + \sum_j \left[i s \frac{2J^2 J_{-1}^2(\alpha)}{\omega} c_{2j+2}^\dagger c_{2j} + \text{H.c.} \right] \\ & - i\lambda \sum_j c_{2j}^\dagger c_{2j}. \end{aligned} \quad (9)$$

The Hamiltonian \mathcal{H}_{eff} in Eq. (9) describes an effective 1D lattice in the presence of both nearest-neighbor and next-nearest-neighbor hoppings, forming a zigzag lattice [see Fig. 3]. Moreover, a $\pi/2$ magnetic flux threads through each triangular plaquette in clockwise and counter-clockwise directions for $\phi = 0$ and $\phi = \pi$ due to the complex next-nearest-neighbor hopping in Eq. (9). Such a nonzero flux leads to opposite particle transports along the odd and even lattice sites^{35,70,71}. Due to the larger loss for the even sites, the particle transport along the odd sites are favored, and the backflow on even sites is suppressed. This leads to skin modes at right and left boundaries for $\phi = 0$ and $\phi = \pi$, respectively.

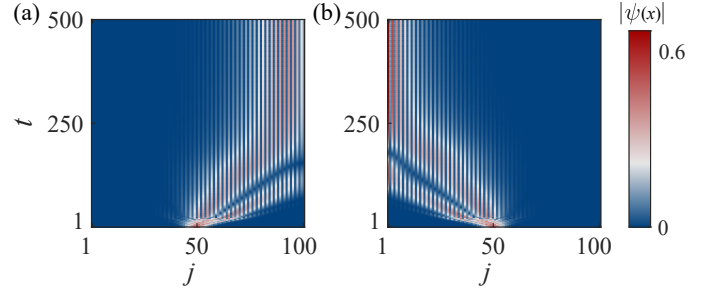


FIG. 5. Dynamical localization of the periodically-driven dissipative system with (a) $\phi = 0$, and (b) $\phi = \pi$, respectively. The initial states are chosen as the Gaussian wavepacket $|\psi_0\rangle = [\psi_0(1), \psi_0(2), \dots, \psi_0(L)]^T$ with $\psi_0(j) = \exp[-(j - j_0)^2/2\sigma^2]/\mathcal{N}$ centered at the site $j_0 = L/2$. Here we choose the width of the wavepacket $\sigma = 5$. The wavepackets at every time have been renormalized. The other parameters used are $\alpha = 1.5$, $\omega = 3\pi$, $\lambda/J = 1$, and $L = 100$.

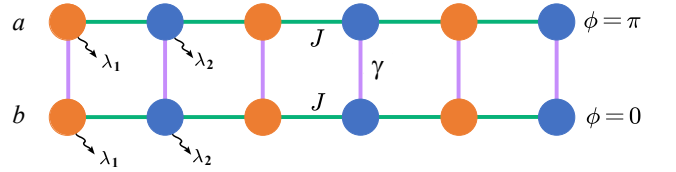


FIG. 6. Schematic showing the lattice ladder of ultracold atoms for realizing critical NHSE. For each leg a or b of the ladder, the optical lattice has the same structure as the one in Fig. 1, which is periodically modulated and staggered with alternating loss λ_1 and λ_2 with $\lambda = \lambda_2 - \lambda_1$. Along the rung, driving phases are set as $\phi = 0$ and $\phi = \pi$, respectively. γ is the hopping strength along the rung.

C. Robustness Against Disorder

The intrinsic topological nature of the NHSE in periodically-driven dissipative ultracold-atom system indicates its robust against local disorders. Here, we consider to introduce the onsite disordered potential into the periodically-driven dissipative system with the system Hamiltonian reading

$$\mathcal{H}_{\text{tot}}(t) = \mathcal{H}(t) + \mathcal{H}_{\text{dis}} = \mathcal{H}(t) + \sum_{j=1}^L U_j n_j. \quad (10)$$

where U_j denotes the onsite random potential, uniformly sampled in $\in [-W/2, W/2]$ with W denoting the disorder strength.

Figure 4 shows the complex quasienergy spectra under OBC and PBC, and the corresponding density distributions of the Floquet Hamiltonian \mathcal{H}_F in the presence of the onsite random potential with the disorder strength $W = 5$ for $\phi = 0$ and $\phi = \pi$. The PBC eigenenergies still form a point gap, encircling all the OBC eigenvalues. All the eigenstates are localized at the right (left) boundary for $\phi = 0$ and $\phi = \pi$, respectively. Therefore, the NHSEs remain in spite

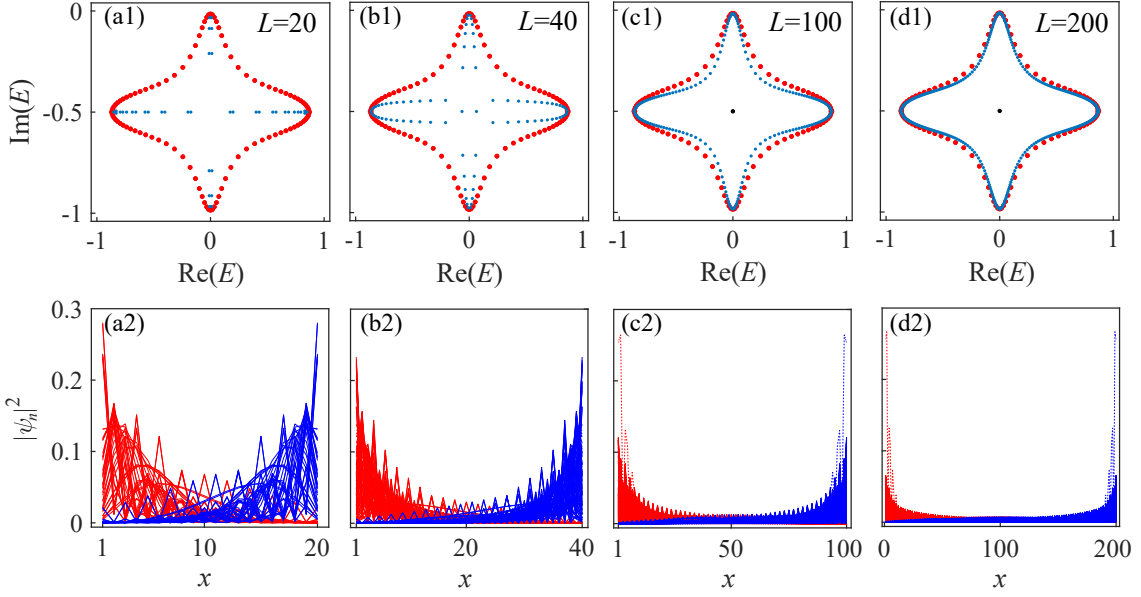


FIG. 7. Complex quasienergy spectrum E_n and corresponding density distributions $|\psi_n|^2$ of the Floquet Hamiltonian \mathcal{H}_L^F of the driving ladder for different size from $L = 20$ to 200 . The red and blue dots indicate the quasienergies under PBC and OBC, respectively. The red and blue lines represent the density distributions $|\psi_n|^2$ of legs a and b , respectively. As the size L increases, the topological in-gap degenerate states (black dots) with zero real parts of complex eigenenergies appear in (c1,d1), and the corresponding state distributions are shown in (c2,d2) with dashed curves. The parameters used are $\alpha = 1.5$, $\omega = 3\pi$, $\lambda/J = 1.0$, and $\gamma/J = 0.005$.

of strong disorder due to the intrinsic non-Hermitian topology of the periodically-driven dissipative ultracold-atom system considered here.

D. Dynamical Localization

The NHSE can be manifested by studying the dynamical evolution. We consider the initial states as the Gaussian wavepacket $|\psi_0\rangle = [\psi_0(1), \psi_0(2), \dots, \psi_0(L)]^T$ with $\psi_0(j) = \exp[-(j - j_0)^2/2\sigma^2]/\mathcal{N}$ centered at the site $j_0 = L/2$, where \mathcal{N} is the normalization constant, and σ denotes the width of the wavepacket. The wavefunction at time t can be obtained by numerically calculating $|\psi(t)\rangle = \mathcal{T} \exp\left(-i \int_0^t \mathcal{H}(\tau) d\tau\right) |\psi_0\rangle$.

We calculate the time-dependent density distributions of the periodically-driven dissipative ultracold-atom system for $\phi = 0$ and $\phi = \pi$, as shown in Fig. 5. Due to the nonreciprocal nature of the considered system, as analyzed above, the wavepacket is finally localized towards the right and left boundary for $\phi = 0$ and $\phi = \pi$, respectively.

III. FLOQUET-INDUCED CRITICAL NON-HERMITIAN SKIN EFFECT

The NHSE can induce a novel critical behavior without its Hermitian counterpart, dubbed the critical NHSE²⁶.

That is, when two non-Hermitian systems with different skin lengths are coupled together, the energy spectrum discontinuously jump across a critical point in the thermodynamic limit. The critical skin effects have been studied in the static systems^{26,27,72,73}. Here, we will show such a critical behavior can be also observed in the driving system.

To study Floquet-induced critical NHSE, we consider the quasi-one-dimensional ladder of ultracold atoms, as shown in Fig. 6. For each leg a or b of the ladder, the optical lattice has the same structure as the one in Fig. 1, which is periodically modulated and staggered with alternating loss λ_1 and λ_2 . Along the rung, driving phases are set as $\phi = 0$ and $\phi = \pi$, respectively. The Hamiltonian of the driving ladder is written in the rotating frame of reference (see Appendix B) as

$$\begin{aligned} \mathcal{H}_L(t) = & - \sum_{j=1}^{L/2} \left(J_-^* a_{2j}^\dagger a_{2j-1} + J_+^* b_{2j}^\dagger b_{2j-1} + \text{H.c.} \right) \\ & - \sum_{j=1}^{L/2-1} \left(J_+ a_{2j+1}^\dagger a_{2j} + J_- b_{2j+1}^\dagger b_{2j} + \text{H.c.} \right) \\ & - \sum_{j=1}^{L/2} i\lambda \left(a_{2j}^\dagger a_{2j} + b_{2j}^\dagger b_{2j} \right) \\ & - \sum_{j=1}^L \gamma \left(a_j^\dagger b_j + \text{H.c.} \right), \end{aligned} \quad (11)$$

where $J_{\pm} = J e^{i\alpha \cos(\omega t \pm \frac{\pi}{4})}$ represents the hopping strength for the leg a and b , λ indicates onsite dissipation with $\lambda = \lambda_2 - \lambda_1$, and γ is the hopping strength along the rung. The Floquet Hamiltonian \mathcal{H}_L^F of the ladder is defined as $U(T) = \mathcal{T} e^{-i \int_0^T \mathcal{H}_L(t') dt'} = e^{-i \mathcal{H}_L^F T}$.

Figure 7 shows the complex quasienergy spectrum and corresponding density distributions of \mathcal{H}_L^F for different sizes L . The PBC spectrum (red dots) is not sensitive to the system size, while the OBC spectrum (blue dots) changes remarkably as the size L of the coupled chain increases from $L = 20$ to 200 in spite of the weak coupling strength between two chains with $\gamma/J = 0.005$. For the small size $L = 20$, the OBC spectrum of the coupled chains mostly resembles the one of respective single chain in Fig. 2(d1,e1). As the size L increases, the OBC spectrum changes, and the bulk OBC spectrum approaches the PBC spectrum of the coupled chain at the large size $L = 200$ [see Fig. 7(d1)]. Moreover, the energy spectrum in the large-size coupled chains under OBC discontinuously jumps across the critical point $\gamma/J = 0$. Therefore, the critical skin effect occurs in the periodically-driven ladder.

Mostly remarkably, the critical skin effect can be manifested by the size-dependent topological phase crossovers. For $\gamma/J = 0$, the system is decoupled into two topologically trivial chains. While, for the nonzero coupling strength $\gamma/J \neq 0$, the momentum-space Hamiltonian $H_L(k, t)$ in Eq. (11) respects chiral symmetry, which supports topological boundary modes (see details in Appendix D). As shown in Fig. 7(a1-d1), there exist no in-gap states for the small size of the ladder [see Fig. 7(a1,b1)]. However, as the size increases, topological degenerate in-gap states appear [see black dots in Fig. 7(c1,d1)]. These in-gap states are localized at the system's boundaries [see Fig. 7(c2, d2)]. In experiments, we can observe the critical non-Hermitian skin effects by directly detecting the topological phase crossovers of the size-dependent in-gap boundary state. In ultracold atoms⁷⁴⁻⁷⁸, the interface boundary between topologically trivial and nontrivial chains can be created by introducing a much large potential step (see details in Appendix D).

IV. CONCLUSION

We have shown theoretically that the NHSE can occur in a periodically-driven ultracold atoms in the presence of the staggered atomic loss. The NHSE is characterized by the winding number, which is quite robust against the disorder. The underlying mechanism governing periodic-drive-induced NHSE is provided by considering Floquet-Magnus expansion in the high-frequency approximation. Moreover, we propose to observe the critical skin effect with the appearance of size-dependent topological in-gap modes by coupling two periodically-driven chains with different driving phases. Our approach can be easily implemented in ultracold atoms based on Floquet

engineering. Floquet engineering has emerged as a powerful experimental method for the realization of novel quantum systems in ultracold-atom systems. Our work paves the way for further studies of the NHSE and its interplay with many-body statistics and interactions in ultracold-atom systems.

ACKNOWLEDGMENTS

T.L. acknowledges the support from Introduced Innovative Team Project of Guangdong Pearl River Talents Program (Grant No. 2021ZT09Z109), the Fundamental Research Funds for the Central Universities (Grant No. 2023ZYGXZR020), National Natural Science Foundation of China (Grant No. 12274142), and the Startup Grant of South China University of Technology (Grant No. 20210012).

Appendix A: Realization of Floquet Hamiltonian in Ultracold atoms

In this Appendix, we provide some details to realize the dissipative Floquet Hamiltonian $\mathcal{H}_p(t) = \mathcal{H}_0 + \mathcal{H}_d(t)$ in Eqs. (1) and (2), which consist of the periodically-modulated staggered onsite potential and tilted potential and the staggered dissipation rates λ_1 and $\lambda_2 = \lambda_1 + \lambda$ at odd and even sites.

As shown in Fig. 8(a), in the experimental setting, the one-dimensional dynamical optical superlattice (along the x direction) in the presence of the periodically-modulated staggered onsite potential can be created by superimposing a stationary lattice (i.e., the short lattice) with a period of λ_S and a dynamical interferometric lattice (i.e., the long lattice) with a period of $\lambda_L = 2\lambda_S$ ⁷⁹⁻⁸¹. The phase of the dynamical interferometric lattice is periodically driven in time and controlled by a Michelson interferometer. The strong confinement along the y and z directions provided by other optical lattices. The dynamical superlattice potential is written as

$$V_1(x, y, z, t) = -V_S(t) \cos^2(k_S x) - V_L(t) \cos^2[k_S x/2 - \varphi(t)], \quad (\text{A1})$$

where V_S and V_L is the depth of the short and long lattice controlled by the respective laser powers, $k_S = 2\pi/\lambda_S$ is the wave vector and $\varphi(t)$ is the phase difference between the two lattice controlled by changing the optical path difference between the two interfering beams⁷⁹⁻⁸¹. The ultracold atomic gases are loaded into this dynamically controlled optical superlattice, and prepared in the first band. The band gap between the first and the higher-level bands are fairly large at each well, we can focus on only the first band⁷⁹⁻⁸¹. Then, in the tight-binding limit, we can achieve periodically-modulated staggered onsite potential in the second term of the right side of the Hamiltonian $\mathcal{H}_d(t)$ in Eq. (2).

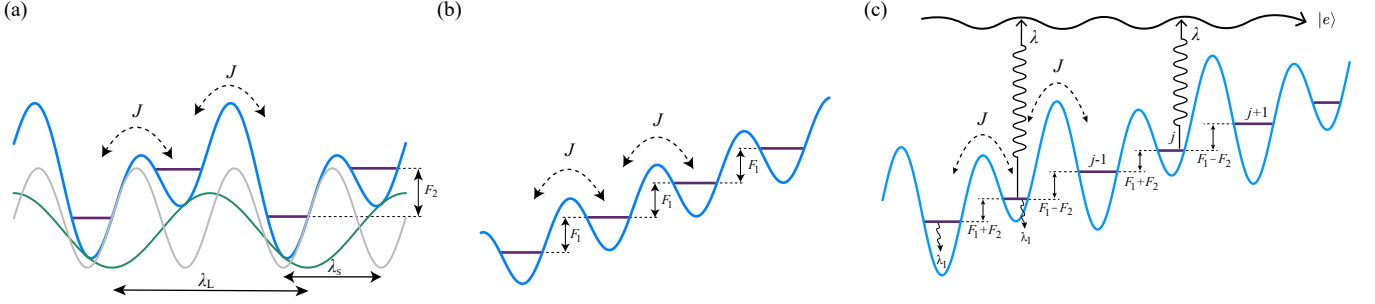


FIG. 8. Schematic showing the dynamical superlattice potential to realize the periodically-driven Hamiltonian $\mathcal{H}_p(t) = \mathcal{H}_0 + \mathcal{H}_d(t)$. The periodically-modulated potential $\mathcal{H}_d(t)$ consists of the time-dependent staggered onsite potential in (a), and time-dependent tiled onsite potential in (b). (a) The one-dimensional dynamical optical superlattice with the time-dependent staggered onsite potential is created by superimposing a stationary lattice and a dynamical one with different periodicities. (b) An additional time-periodic modulation of the lattice position is superimposed to create the time-dependent tilted potential. (c) When the atoms are prepared in the first-band state, the staggered dissipation rates λ_1 and $\lambda_2 = \lambda_1 + \lambda$ at odd and even sites in \mathcal{H}_0 are realized via exciting the state in the first band at even sites to the higher-level state $|e\rangle$, where the additional dissipation λ is controlled by the intensity of the external optical beam.

Secondly, in order to construct the periodically-modulated tilted potential, we superimpose an additional drive consisting of a time-periodic modulation of the lattice position x with the frequency ω , as shown in Fig. 8(b). The time-periodic modulation of the lattice site has the form

$$V_2(x, y, z, t) = -V(x - A \cos(\omega t + \phi_c)), \quad (\text{A2})$$

where A is the modulation amplitude, and ϕ_c is phase. Such a tilted potential under periodical-modulation (i.e., the time-dependent force) has been experimentally realized in ultracold-atom systems^{62,82}. Then, in the tight-binding limit, we can achieve periodically-modulated tilted potential in the first term of the right side of in the Hamiltonian $\mathcal{H}_d(t)$ in Eq. (2).

Finally, when the atoms are prepared in the first-band state, the staggered dissipation rates λ_1 and $\lambda_2 = \lambda_1 + \lambda$ at odd and even sites in \mathcal{H}_0 are realized via exciting the state in the first band at even sites to the higher-level state $|e\rangle$, where the additional dissipation λ is controlled by the intensity of the external optical beam [see Fig. 8(c)]. In order to selectively excite the atoms at even sites, we can utilize the ground-state hyperfine states in the combination of the Raman-assisted hopping between adjacent sites. To be specific, we consider ultracold atoms with two internal states, e.g., spin up and spin down. The spin-up states at the odd sites are hopped to spin-down states at the even sites using Raman-assisted hopping. Then, the staggered dissipation can be realized by exciting all the spin-down states at the even sites to higher-level states. Note that the loss control using different internal states in optical lattice of ultracold atoms have been experimentally reported^{38,52,83,84}.

Appendix B: Unitary transformation of Floquet Hamiltonian

As shown in the main text, we construct the periodically-driven Hamiltonian $\mathcal{H}_p(t) = \mathcal{H}_0 + \mathcal{H}_d(t)$, with

$$\mathcal{H}_0 = -J \sum_{j=1}^{L-1} (c_{j+1}^\dagger c_j + \text{H.c.}) - i\lambda \sum_{j=1}^{L/2} n_{2j}, \quad (\text{B1})$$

$$\mathcal{H}_d(t) = \sum_{j=1}^L F \left[\cos(\omega t + \phi) j + \sin(\omega t) \frac{3 + (-1)^j}{2} \right] n_j, \quad (\text{B2})$$

where, without loss of generality, we set $\lambda_1 = 0$.

After performing a unitary transformation $\mathcal{H}(t) = \mathcal{U} \mathcal{H}_p(t) \mathcal{U}^\dagger - i \mathcal{U} \partial_t \mathcal{U}^\dagger$, with $\mathcal{U}(t)$ being written as

$$\mathcal{U}(t) = e^{i \left(\frac{F}{\omega} \sin(\omega t + \phi) \sum_{j=1}^L j n_j - \frac{F}{\omega} \cos(\omega t) \sum_{j=1}^L \frac{3 + (-1)^j}{2} n_j \right)}, \quad (\text{B3})$$

we achieve the periodically-driven Hamiltonian as

$$\begin{aligned} \mathcal{H}(t) = & \sum_{j=1}^{L/2} \left[\left(u c_{2j}^\dagger c_{2j-1} + \text{H.c.} \right) - i \lambda n_{2j} \right] \\ & - \sum_{j=1}^{L/2-1} \left(v c_{2j+1}^\dagger c_{2j} + \text{H.c.} \right), \end{aligned} \quad (\text{B4})$$

where

$$u = -J e^{i \sqrt{2} \alpha \cos(\frac{\phi}{2} + \frac{\pi}{4}) \sin(\omega t + \frac{\phi}{2} - \frac{\pi}{4})}, \quad (\text{B5})$$

$$v = -J e^{i \sqrt{2} \alpha \sin(\frac{\phi}{2} + \frac{\pi}{4}) \cos(\omega t + \frac{\phi}{2} - \frac{\pi}{4})}, \quad (\text{B6})$$

with $\alpha = \sqrt{2} F / \omega$.

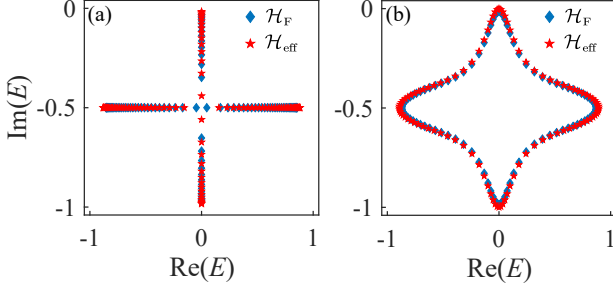


FIG. 9. Complex quasienergy spectrum E_n calculated using the Floquet Hamiltonian \mathcal{H}_F (blue diamond dots) and effective Hamiltonian \mathcal{H}_{eff} (red star dots) in the high-frequency limit under OBC (a) and PBC (b). The parameters used are $\alpha = 1.5$, $\omega = 3\pi$, $\lambda/J = 1$, and $L = 100$.

Appendix C: Effective Hamiltonian via Floquet-Magnus Expansion

In this appendix, we provide some details to obtain the time-independent effective Hamiltonian \mathcal{H}_{eff} by applying the Floquet-Magnus expansion^{67–69} in the high-frequency approximation ($\omega \gg J, F$). Up to the first-order approximation, the effective Hamiltonian is written as

$$\mathcal{H}_{\text{eff}} = \sum_{\mu=0,1} \mathcal{H}_{\text{eff}}^{(\mu)}, \quad (\text{C1})$$

where

$$\mathcal{H}_{\text{eff}}^{(0)} = \mathcal{H}_0, \quad \mathcal{H}_{\text{eff}}^{(1)} = \sum_{m \neq 0} \frac{[\mathcal{H}_{-m}, \mathcal{H}_m]}{2m\omega}, \quad (\text{C2})$$

with $\mathcal{H}_m = T^{-1} \int_0^T \mathcal{H}(t) e^{im\omega t} dt$.

We first derive the effective high-frequency Hamiltonian for the real-space model $\mathcal{H}(t)$ in Eq. (3) of the main text. For $m \neq 0$ and $\phi = 0, \pi$, \mathcal{H}_m reads

$$\begin{aligned} \mathcal{H}_m = & \sum_j \left[P_m\left(\frac{3\pi}{4}\right) c_{2j}^\dagger c_{2j-1} + P_m\left(-\frac{\pi}{4}\right) c_{2j-1}^\dagger c_{2j} \right] \\ & + \sum_j \left[P_m\left(\frac{\pi}{4}\right) c_{2j+1}^\dagger c_{2j} + P_m\left(-\frac{3\pi}{4}\right) c_{2j}^\dagger c_{2j+1} \right], \end{aligned} \quad (\text{C3})$$

where

$$P_m(\Phi) = -Ji^{-m} J_{-m}(\alpha) e^{ims\Phi}, \quad (\text{C4})$$

with $J_m(\alpha)$ being the Bessel function of the first kind, and $s = 1$ (-1) corresponding to $\phi = 0$ (π).

According to Eqs. (C1–C3), we obtain the effective

time-independent Hamiltonian \mathcal{H}_{eff} of $\mathcal{H}(t)$ as

$$\begin{aligned} \mathcal{H}_{\text{eff}} = & - \sum_j \left[J J_0(\alpha) c_{2j}^\dagger c_{2j-1} + J J_0(\alpha) c_{2j+1}^\dagger c_{2j} + \text{H.c.} \right] \\ & - \sum_{j=1} \left[is \frac{2J^2 J_{-1}^2(\alpha)}{\omega} c_{2j+1}^\dagger c_{2j-1} + \text{H.c.} \right] \\ & + \sum_j \left[is \frac{2J^2 J_{-1}^2(\alpha)}{\omega} c_{2j+2}^\dagger c_{2j} + \text{H.c.} \right] \\ & - i\lambda \sum_j c_{2j}^\dagger c_{2j}, \end{aligned} \quad (\text{C5})$$

where only the term with $m = 1$ is considered in the high-frequency limit in Eq. (C2).

We now derive the effective high-frequency Hamiltonian for the momentum-space Hamiltonian $\mathcal{H}(k, t)$. We rewrite $\mathcal{H}(t)$ in Eq. (3) as

$$\mathcal{H}(t) = \sum_j \left[\left(u c_{j,B}^\dagger c_{j,A} + v c_{j+1,A}^\dagger c_{j,B} + \text{H.c.} \right) - i\lambda n_{j,B} \right]. \quad (\text{C6})$$

Then, the momentum-space Hamiltonian $\mathcal{H}(k, t)$ is written as

$$\begin{aligned} \mathcal{H}(k, t) = & \sum_k \left[\left(u^* + v e^{-ik} \right) c_{k,A}^\dagger c_{k,B} + \text{H.c.} \right] \\ & - i\lambda \sum_k c_{k,B}^\dagger c_{k,B}, \end{aligned} \quad (\text{C7})$$

where A and B denote two sublattice sites in the unit cell due to the staggered loss.

For $m \neq 0$ and $\phi = 0, \pi$, $\mathcal{H}_m(k)$ reads

$$\mathcal{H}_m(k) = \sum_k \left[Q_{m,1}(k) c_{k,A}^\dagger c_{k,B} + Q_{m,2}(k) c_{k,B}^\dagger c_{k,A} \right], \quad (\text{C8})$$

where

$$Q_{m,1}(k) = -Ji^{-m} J_{-m}(\alpha) \left(e^{-ism\frac{\pi}{4}} + e^{ism\frac{\pi}{4}} e^{-ik} \right), \quad (\text{C9})$$

$$Q_{m,2}(k) = -Ji^{-m} J_{-m}(\alpha) \left(e^{ism\frac{3\pi}{4}} + e^{-ism\frac{3\pi}{4}} e^{ik} \right). \quad (\text{C10})$$

According to Eqs. (C1) and (C8), we obtain the effective time-independent Hamiltonian $\mathcal{H}_{\text{eff}}(k)$ of $\mathcal{H}(k, t)$ as

$$\begin{aligned} \mathcal{H}_{\text{eff}}(k) = & - \sum_k \left[J J_0(\alpha) \left(1 + e^{-ik} \right) c_{k,A}^\dagger c_{k,B} + \text{H.c.} \right] \\ & - s \frac{2J^2 J_{-1}^2(\alpha)}{\omega} \sum_k \sin(k) \left(c_{k,A}^\dagger c_{k,A} - c_{k,B}^\dagger c_{k,B} \right) \\ & - i\lambda \sum_k c_{k,B}^\dagger c_{k,B}, \end{aligned} \quad (\text{C11})$$

with only the term with $m = 1$ is considered in the high-frequency limit in Eq. (C2).

In Fig. 9, we plot the OBC and PBC spectra, calculated using the Floquet Hamiltonian \mathcal{H}_F (blue diamond dots) and effective Hamiltonian \mathcal{H}_{eff} (red star dots). The effective Hamiltonian in the high-frequency limit shows a good approximation to the Floquet Hamiltonian.

Appendix D: Topological Phase of Periodically-Driven Ladder

In this appendix, we show more details of topological phases of the ladder system (see Fig. 6), which are protected by the energy gap and chiral symmetry. The momentum-space Hamiltonian of the ladder is written as $\mathcal{H}_L(k, t) = \sum_k \Psi_k^\dagger H_L(k, t) \Psi_k$, with $\Psi_k = (a_{k,A}, a_{k,B}, b_{k,A}, b_{k,B})^T$, where A and B denote sublattices along each leg, as shown by yellow and blue filled circles in Fig. 6, and $H_L(k, t)$ is

$$H_L(k, t) = \begin{pmatrix} 0 & -J_- - J_+ e^{-ik} & -\gamma & 0 \\ -J_-^* - J_+^* e^{ik} & -i\lambda & 0 & -\gamma \\ -\gamma & 0 & 0 & -J_+ - J_- e^{-ik} \\ 0 & -\gamma & -J_+^* - J_-^* e^{ik} & -i\lambda \end{pmatrix}. \quad (\text{D1})$$

The Floquet Hamiltonian $H_L^F(k)$ of the ladder in momentum space is defined as $U(T) = \mathcal{T} e^{-i \int_0^T H_L(k, t') dt'} = e^{-i H_L^F(k) T}$.

The Hamiltonian $H_L(k, t)$ respects chiral symmetry $S H_L(k, t) S^{-1} = -H_L^\dagger(k, -t)$, where $S = \sigma_y \tau_z$, with Pauli matrices $\sigma_{0,x,y,z}$ and $\tau_{0,x,y,z}$ acting on the sublattices (A, B) in each leg and legs (a, b) degrees of freedom, respectively. As shown in Fig. 10(a,b), the Floquet Hamiltonian $H_L^F(k)$ has a line gap. According to topological classification of Floquet non-Hermitian system⁸⁵, it supports a topological nontrivial phase. Figure 10(c,d) clearly shows the degenerate in-gap boundary modes.

In experiments, we can observe the critical non-Hermitian skin effects by directly detecting the topological phase crossovers of the size-dependent in-gap boundary state. In ultracold atoms, the interface

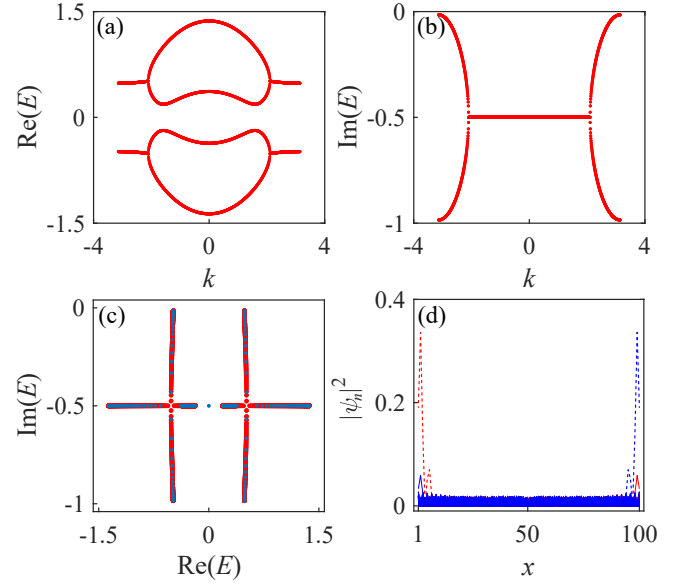


FIG. 10. (a) Real part and (b) imaginary part of complex quasienergy spectrum of the Floquet Hamiltonian $\mathcal{H}_L^F(k)$ of $\mathcal{H}_L(k, t)$ in the momentum space. (c) Complex quasienergy spectrum E_n of the ladder under PBC (red dots) and OBC (blue dots). (d) The corresponding density distribution of the ladder under OBC. The red and blue lines represent states in legs a and b , respectively. The dashed lines denote the topological in-gap boundary states. The parameters are chosen as $\alpha = 1.5$, $\omega = 3\pi$, $\lambda/J = 1$, $\gamma/J = 0.5$, and $L = 100$.

boundary between topologically trivial and nontrivial chains can be created by illuminating a selected area of the lattice with a large optical potential^{74–78}. As shown in Fig. 11(a), the middle ladder with the size L_2 is sandwiched by two ladders with lengths L_1 and L_3 in the presence of the much large onsite potential Δ and $-\Delta$ in chains a and b . The left and right ladders are topologically trivial for large Δ due to the broken chiral symmetry. We calculate the complex-eigenenergy spectrum and the corresponding density distributions for $L_2 = 40$ [see Fig. 11(b,c)] and $L_2 = 40$ [see Fig. 11(d,e)]. The results indicate that the eigenenergy spectrum and state density distribution of the middle ladder are largely separated from those of the left and right ladders, and have the same features as the single ladder under OBCs (see Fig. 7) for large Δ .

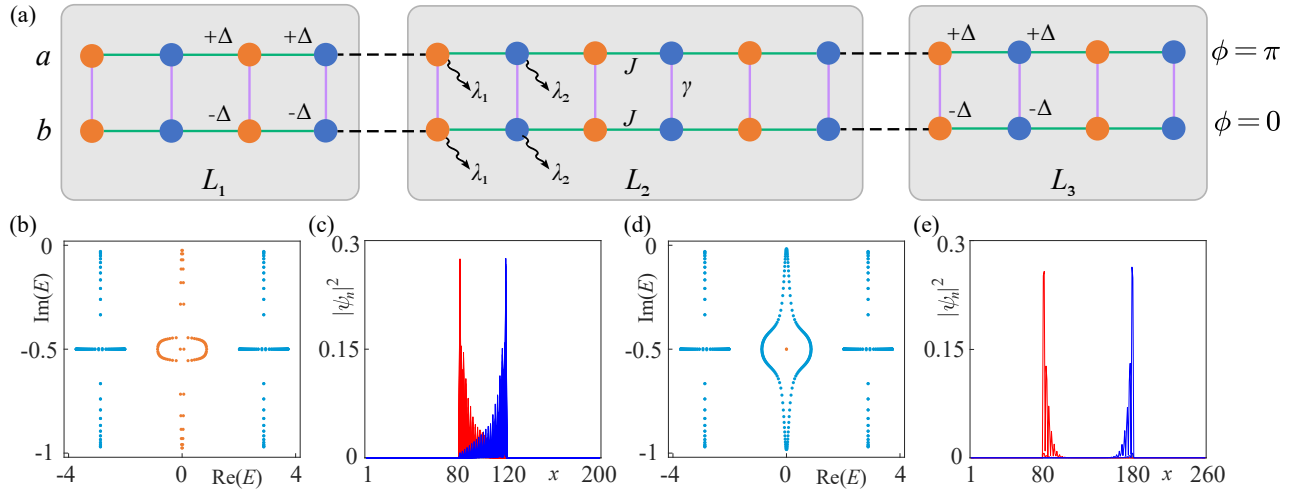


FIG. 11. (a) A middle ladder with the size L_2 is sandwiched by two ladders with lengths L_1 and L_3 in the presence of the much large onsite potential Δ and $-\Delta$ in chains a and b . (b) Complex-eigenenergy spectrum and (c) the corresponding density distributions of states indicated by red dots in (b) for $L_2 = 40$. (d) Complex-eigenenergy spectrum and (e) the density distributions of the topological in-gap states ($E = -0.5i$) indicated by red dots in (d) for $L_2 = 100$. The parameters used are $\alpha = 1.5$, $\omega = 3\pi$, $\lambda/J = 1.0$, and $\gamma/J = 0.005$.

* E-mail: liutao0716@scut.edu.cn

† E-mail: yangzm@scut.edu.cn

- ¹ V. V. Konotop, J. Yang, and D. A. Zezyulin, “Nonlinear waves in \mathcal{PT} -symmetric systems,” *Rev. Mod. Phys.* **88**, 035002 (2016).
- ² Tony E. Lee, “Anomalous edge state in a non-Hermitian lattice,” *Phys. Rev. Lett.* **116**, 133903 (2016).
- ³ D. Leykam, K. Y. Bliokh, C. Huang, Y. D. Chong, and F. Nori, “Edge modes, degeneracies, and topological numbers in non-Hermitian systems,” *Phys. Rev. Lett.* **118**, 040401 (2017).
- ⁴ Y. Xu, S. T. Wang, and L. M. Duan, “Weyl exceptional rings in a three-dimensional dissipative cold atomic gas,” *Phys. Rev. Lett.* **118**, 045701 (2017).
- ⁵ Z. Gong, Y. Ashida, K. Kawabata, K. Takasan, S. Higashikawa, and M. Ueda, “Topological phases of non-Hermitian systems,” *Phys. Rev. X* **8**, 031079 (2018).
- ⁶ R. El-Ganainy, K. G. Makris, M. Khajavikhan, Z. H. Musslimani, S. Rotter, and D. N. Christodoulides, “Non-Hermitian physics and PT symmetry,” *Nat. Phys.* **14**, 11 (2018).
- ⁷ S. Yao and Z. Wang, “Edge states and topological invariants of non-Hermitian systems,” *Phys. Rev. Lett.* **121**, 086803 (2018).
- ⁸ K. Zhang, Z. Yang, and C. Fang, “Correspondence between winding numbers and skin modes in non-Hermitian systems,” *Phys. Rev. Lett.* **125**, 126402 (2020).
- ⁹ K. Yokomizo and S. Murakami, “Non-Bloch band theory of non-Hermitian systems,” *Phys. Rev. Lett.* **123**, 066404 (2019).
- ¹⁰ S. Yao, F. Song, and Z. Wang, “Non-Hermitian Chern bands,” *Phys. Rev. Lett.* **121**, 136802 (2018).
- ¹¹ F. K. Kunst, E. Edvardsson, J. C. Budich, and E. J. Bergholtz, “Biorthogonal bulk-boundary correspondence in non-Hermitian systems,” *Phys. Rev. Lett.* **121**, 026808 (2018).
- ¹² T. Liu, Y.-R. Zhang, Q. Ai, Z. Gong, K. Kawabata, M. Ueda, and F. Nori, “Second-order topological phases in non-Hermitian systems,” *Phys. Rev. Lett.* **122**, 076801 (2019).
- ¹³ L. Zhou and J. Gong, “Non-Hermitian Floquet topological phases with arbitrarily many real-quasienergy edge states,” *Phys. Rev. B* **98**, 205417 (2018).
- ¹⁴ L. Zhou, “Dynamical characterization of non-Hermitian Floquet topological phases in one dimension,” *Phys. Rev. B* **100**, 184314 (2019).
- ¹⁵ A. Banerjee and A. Narayan, “Controlling exceptional points with light,” *Phys. Rev. B* **102**, 205423 (2020).
- ¹⁶ F. Song, S. Yao, and Z. Wang, “Non-Hermitian skin effect and chiral damping in open quantum systems,” *Phys. Rev. Lett.* **123**, 170401 (2019).
- ¹⁷ J. Y. Lee, J. Ahn, H. Zhou, and A. Vishwanath, “Topological correspondence between Hermitian and non-Hermitian systems: Anomalous dynamics,” *Phys. Rev. Lett.* **123**, 206404 (2019).
- ¹⁸ K. Kawabata, T. Bessho, and M. Sato, “Classification of exceptional points and non-Hermitian topological semimetals,” *Phys. Rev. Lett.* **123**, 066405 (2019).
- ¹⁹ C. H. Lee and R. Thomale, “Anatomy of skin modes and topology in non-Hermitian systems,” *Phys. Rev. B* **99**, 201103 (2019).
- ²⁰ Z. Y. Ge, Y. R. Zhang, T. Liu, S. W. Li, H. Fan, and F. Nori, “Topological band theory for non-Hermitian systems from the Dirac equation,” *Phys. Rev. B* **100**, 054105 (2019).
- ²¹ H. Zhou and J. Y. Lee, “Periodic table for topological bands with non-Hermitian symmetries,” *Phys. Rev. B* **99**, 235112 (2019).
- ²² H. Zhao, X. Qiao, T. Wu, B. Midya, S. Longhi, and L. Feng, “Non-Hermitian topological light steering,”

- Science **365**, 1163 (2019).
- ²³ K. Kawabata, K. Shiozaki, M. Ueda, and M. Sato, “Symmetry and topology in non-Hermitian physics,” *Phys. Rev. X* **9**, 041015 (2019).
 - ²⁴ D. S. Borgnia, A. J. Kruchkov, and R.-J. Slager, “Non-Hermitian boundary modes and topology,” *Phys. Rev. Lett.* **124**, 056802 (2020).
 - ²⁵ T. Liu, J. J. He, T. Yoshida, Z.-L. Xiang, and F. Nori, “Non-Hermitian topological Mott insulators in one-dimensional fermionic superlattices,” *Phys. Rev. B* **102**, 235151 (2020).
 - ²⁶ L. Li, C. H. Lee, S. Mu, and J. Gong, “Critical non-Hermitian skin effect,” *Nat. Commun.* **11** (2020), 10.1038/s41467-020-18917-4.
 - ²⁷ K. Yokomizo and S. Murakami, “Scaling rule for the critical non-Hermitian skin effect,” *Phys. Rev. B* **104**, 165117 (2021).
 - ²⁸ Y. Ashida, Z. Gong, and M. Ueda, “Non-Hermitian physics,” *Adv. Phys.* **69**, 249 (2020).
 - ²⁹ K. Kawabata, M. Sato, and K. Shiozaki, “Higher-order non-Hermitian skin effect,” *Phys. Rev. B* **102**, 205118 (2020).
 - ³⁰ N. Okuma, K. Kawabata, K. Shiozaki, and M. Sato, “Topological origin of non-Hermitian skin effects,” *Phys. Rev. Lett.* **124**, 086801 (2020).
 - ³¹ Y. Yi and Z. Yang, “Non-Hermitian skin modes induced by on-site dissipations and chiral tunneling effect,” *Phys. Rev. Lett.* **125**, 186802 (2020).
 - ³² T. Liu, J. J. He, Z. Yang, and F. Nori, “Higher-order Weyl-exceptional-ring semimetals,” *Phys. Rev. Lett.* **127**, 196801 (2021).
 - ³³ L. Li, C. H. Lee, and J. Gong, “Impurity induced scale-free localization,” *Commun. Phys.* **4** (2021), 10.1038/s42005-021-00547-x.
 - ³⁴ E. J. Bergholtz, J. C. Budich, and F. K. Kunst, “Exceptional topology of non-Hermitian systems,” *Rev. Mod. Phys.* **93**, 015005 (2021).
 - ³⁵ Y. Li, C. Liang, C. Wang, C. Lu, and Y.-C. Liu, “Gain-loss-induced hybrid skin-topological effect,” *Phys. Rev. Lett.* **128**, 223903 (2022).
 - ³⁶ K. Zhang, Z. Yang, and C. Fang, “Universal non-Hermitian skin effect in two and higher dimensions,” *Nat. Commun.* **13** (2022), 10.1038/s41467-022-30161-6.
 - ³⁷ K. Li and Y. Xu, “Non-Hermitian absorption spectroscopy,” *Phys. Rev. Lett.* **129**, 093001 (2022).
 - ³⁸ Z. Ren, D. Liu, E. Zhao, C. He, K. K. Pak, J. Li, and G.-B. Jo, “Chiral control of quantum states in non-Hermitian spin-orbit-coupled fermions,” *Nat. Phys.* **18**, 385 (2022).
 - ³⁹ K. Kawabata, T. Numasawa, and S. Ryu, “Entanglement phase transition induced by the non-Hermitian skin effect,” *Phys. Rev. X* **13**, 021007 (2023).
 - ⁴⁰ K. Zhang, C. Fang, and Z. Yang, “Dynamical degeneracy splitting and directional invisibility in non-Hermitian systems,” *Phys. Rev. Lett.* **131**, 036402 (2023).
 - ⁴¹ C.-A. Li, B. Trauzettel, T. Neupert, and S.-B. Zhang, “Enhancement of second-order non-Hermitian skin effect by magnetic fields,” *Phys. Rev. Lett.* **131**, 116601 (2023).
 - ⁴² X. Li, J. Liu, and T. Liu, “Localization-delocalization transitions in non-Hermitian Aharonov-Bohm cages,” *Front. Phys.* **19**, 33211 (2024).
 - ⁴³ N. Okuma and M. Sato, “Non-Hermitian topological phenomena: A review,” *Annu. Rev. Condens. Matter Phys.* **14**, 83 (2023).
 - ⁴⁴ K. Kawabata and S. Ryu, “Nonunitary scaling theory of non-Hermitian localization,” *Phys. Rev. Lett.* **126**, 166801 (2021).
 - ⁴⁵ R. Lin, T. Tai, L. Li, and C. H. Lee, “Topological non-Hermitian skin effect,” *Front. Phys.* **18** (2023), 10.1007/s11467-023-1309-z.
 - ⁴⁶ S. Weidemann, M. Kremer, T. Helbig, T. Hofmann, A. Stegmaier, M. Greiter, R. Thomale, and A. Szameit, “Topological funneling of light,” *Science* **368**, 311 (2020).
 - ⁴⁷ K. Wang, A. Dutt, K. Y. Yang, C. C. Wojcik, J. Vučković, and S. Fan, “Generating arbitrary topological windings of a non-Hermitian band,” *Science* **371**, 1240 (2021).
 - ⁴⁸ Q. Zhou, J. Wu, Z. Pu, J. Lu, X. Huang, W. Deng, M. Ke, and Z. Liu, “Observation of geometry-dependent skin effect in non-Hermitian phononic crystals with exceptional points,” *Nat. Commun.* **14** (2023), 10.1038/s41467-023-40236-7.
 - ⁴⁹ T. Helbig, T. Hofmann, S. Imhof, M. Abdelghany, T. Kiessling, L. W. Molenkamp, C. H. Lee, A. Szameit, M. Greiter, and R. Thomale, “Generalized bulk-boundary correspondence in non-Hermitian topoelectrical circuits,” *Nat. Phys.* **16**, 747 (2020).
 - ⁵⁰ D. Zou, T. Chen, W. He, J. Bao, C. H. Lee, H. Sun, and X. Zhang, “Observation of hybrid higher-order skin-topological effect in non-Hermitian topoelectrical circuits,” *Nat. Commun.* **12** (2021), 10.1038/s41467-021-26414-5.
 - ⁵¹ L. Li, C. H. Lee, and J. Gong, “Topological switch for non-Hermitian skin effect in cold-atom systems with loss,” *Phys. Rev. Lett.* **124**, 250402 (2020).
 - ⁵² Q. Liang, D. Xie, Z. Dong, H. Li, H. Li, B. Gadway, W. Yi, and B. Yan, “Dynamic signatures of non-Hermitian skin effect and topology in ultracold atoms,” *Phys. Rev. Lett.* **129**, 070401 (2022).
 - ⁵³ S. Giorgini, L. P. Pitaevskii, and S. Stringari, “Theory of ultracold atomic Fermi gases,” *Rev. Mod. Phys.* **80**, 1215 (2008).
 - ⁵⁴ D.-W. Zhang, Y.-Q. Zhu, Y. X. Zhao, H. Yan, and S.-L. Zhu, “Topological quantum matter with cold atoms,” *Adv. Phys.* **67**, 253 (2018).
 - ⁵⁵ N. R. Cooper, J. Dalibard, and I. B. Spielman, “Topological bands for ultracold atoms,” *Rev. Mod. Phys.* **91**, 015005 (2019).
 - ⁵⁶ F. Schäfer, T. Fukuhara, S. Sugawa, Y. Takasu, and Y. Takahashi, “Tools for quantum simulation with ultracold atoms in optical lattices,” *Nat. Rev. Phys.* **2**, 411 (2020).
 - ⁵⁷ L. Zhou, H. Li, W. Yi, and X. Cui, “Engineering non-Hermitian skin effect with band topology in ultracold gases,” *Commun. Phys.* **5** (2022), 10.1038/s42005-022-01021-y.
 - ⁵⁸ S. Guo, C. Dong, F. Zhang, J. Hu, and Z. Yang, “Theoretical prediction of a non-Hermitian skin effect in ultracold-atom systems,” *Phys. Rev. A* **106**, L061302 (2022).
 - ⁵⁹ N. Goldman and J. Dalibard, “Periodically driven quantum systems: Effective Hamiltonians and engineered gauge fields,” *Phys. Rev. X* **4**, 031027 (2014).
 - ⁶⁰ N. Goldman, J. C. Budich, and P. Zoller, “Topological quantum matter with ultracold gases in optical lattices,” *Nat. Phys.* **12**, 639 (2016).
 - ⁶¹ A. Eckardt, “Colloquium: Atomic quantum gases in periodically driven optical lattices,” *Rev. Mod. Phys.* **89**, 011004 (2017).
 - ⁶² F. Görg, K. Sandholzer, J. Minguzzi, R. Desbuquois, M. Messer, and T. Esslinger, “Realization of density-

- dependent Peierls phases to engineer quantized gauge fields coupled to ultracold matter,” *Nat. Phys.* **15**, 1161 (2019).
- ⁶³ C. Weitenberg and J. Simonet, “Tailoring quantum gases by Floquet engineering,” *Nat. Phys.* **17**, 1342 (2021).
- ⁶⁴ Y. Li, C. Lu, S. Zhang, and Y.-C. Liu, “Loss-induced Floquet non-Hermitian skin effect,” *Phys. Rev. B* **108**, L220301 (2023).
- ⁶⁵ C. Shu, K. Zhang, and K. Sun, “Loss-induced universal one-way transport in periodically driven systems,” *Phys. Rev. B* **109**, 184302 (2024).
- ⁶⁶ M. S. Rudner and N. H. Lindner, “Band structure engineering and non-equilibrium dynamics in Floquet topological insulators,” *Nature Reviews Physics* **2** (2020), 10.1038/s42254-020-0170-z.
- ⁶⁷ M. Bukov, L. D’Alessio, and A. Polkovnikov, “Universal high-frequency behavior of periodically driven systems: From dynamical stabilization to Floquet engineering,” *Adv. Phys.* **64**, 139 (2015).
- ⁶⁸ A. Eckardt and E. Anisimovas, “High-frequency approximation for periodically driven quantum systems from a Floquet-space perspective,” *New J. Phys.* **17**, 093039 (2015).
- ⁶⁹ T. Mikami, S. Kitamura, K. Yasuda, N. Tsuji, T. Oka, and H. Aoki, “Brillouin-Wigner theory for high-frequency expansion in periodically driven systems: Application to Floquet topological insulators,” *Phys. Rev. B* **93**, 144307 (2016).
- ⁷⁰ W. Zhu and J. Gong, “Hybrid skin-topological modes without asymmetric couplings,” *Phys. Rev. B* **106**, 035425 (2022).
- ⁷¹ H. Cai, J. Liu, J. Wu, Y. He, S.-Y. Zhu, J.-X. Zhang, and D.-W. Wang, “Experimental observation of momentum-space chiral edge currents in room-temperature atoms,” *Phys. Rev. Lett.* **122**, 023601 (2019).
- ⁷² S. M. Rafi-Ul-Islam, Z. B. Siu, H. Sahin, C. H. Lee, and M. B. A. Jalil, “Critical hybridization of skin modes in coupled non-Hermitian chains,” *Phys. Rev. Res.* **4**, 013243 (2022).
- ⁷³ F. Qin, Y. Ma, R. Shen, and C. H. Lee, “Universal competitive spectral scaling from the critical non-Hermitian skin effect,” *Phys. Rev. B* **107**, 155430 (2023).
- ⁷⁴ A. L. Gaunt, T. F. Schmidutz, I. Gotlibovych, R. P. Smith, and Z. Hadzibabic, “Bose-Einstein condensation of atoms in a uniform potential,” *Phys. Rev. Lett.* **110**, 200406 (2013).
- ⁷⁵ N. Goldman, J. Dalibard, A. Dauphin, F. Gerbier, M. Lewenstein, P. Zoller, and I. B. Spielman, “Direct imaging of topological edge states in cold-atom systems,” *PNAS* **110**, 13986 (2013).
- ⁷⁶ L. Chomaz, L. Corman, T. Bienaimé, R. Desbuquois, C. Weitenberg, S. Nascimbène, J. Beugnon, and J. Dalibard, “Emergence of coherence via transverse condensation in a uniform quasi-two-dimensional Bose gas,” *Nat. Commun.* **6**, 6162 (2015).
- ⁷⁷ K. Hueck, N. Luick, L. Sobirey, J. Siegl, T. Lompe, and H. Moritz, “Two-dimensional homogeneous Fermi gases,” *Phys. Rev. Lett.* **120**, 060402 (2018).
- ⁷⁸ C. Braun, R. Saint-Jalm, A. Hesse, J. Arceri, I. Bloch, and M. Aidelsburger, “Real-space detection and manipulation of topological edge modes with ultracold atoms,” *arXiv:2304.01980* (2023), 10.1073/pnas.1300170110.
- ⁷⁹ M. Lohse, C. Schweizer, O. Zilberberg, M. Aidelsburger, and I. Bloch, “A Thouless quantum pump with ultracold bosonic atoms in an optical superlattice,” *Nat. Phys.* **12**, 350 (2015).
- ⁸⁰ S. Nakajima, T. Tomita, S. Taie, T. Ichinose, H. Ozawa, L. Wang, M. Troyer, and Y. Takahashi, “Topological Thouless pumping of ultracold fermions,” *Nat. Phys.* **12**, 296 (2016).
- ⁸¹ S. Nakajima, N. Takei, K. Sakuma, Y. Kuno, P. Marra, and Y. Takahashi, “Competition and interplay between topology and quasi-periodic disorder in Thouless pumping of ultracold atoms,” *Nat. Phys.* **17**, 844 (2021).
- ⁸² R. Desbuquois, M. Messer, F. Görg, K. Sandholzer, G. Jotzu, and T. Esslinger, “Controlling the Floquet state population and observing micromotion in a periodically driven two-body quantum system,” *Phys. Rev. A* **96**, 053602 (2017).
- ⁸³ J. Li, A. K. Harter, J. Liu, L. de Melo, Y. N. Joglekar, and L. Luo, “Observation of parity-time symmetry breaking transitions in a dissipative Floquet system of ultracold atoms,” *Nat. Commun.* **10** (2019), 10.1038/s41467-019-08596-1.
- ⁸⁴ E. Zhao, Z. Wang, C. He, T. F. J. Poon, K. K. Pak, Y.-J. Liu, P. Ren, X.-J. Liu, and G.-B. Jo, “Two-dimensional non-Hermitian skin effect in an ultracold fermi gas,” *arXiv:2311.07931* (2023).
- ⁸⁵ C.-H. Liu, H. Hu, and S. Chen, “Symmetry and topological classification of Floquet non-Hermitian systems,” *Phys. Rev. B* **105**, 214305 (2022).